NOEMA OBSERVATIONS OF CO EMISSION IN ARP 142 AND ARP 238

C. K. Xu[1,2], U. Lisenfeld[3,4], Y. Gao[5,6], F. Renaud[7]

ABSTRACT

Previous studies have shown significant differences in the enhancement of the star-formation rate (SFR) and the star-formation efficiency (SFE = SFR/M_{mol}) between spiral-spiral and spiral-elliptical mergers. In order to shed light on the physical mechanism of these differences, we present NOEMA observations of the molecular gas distribution and kinematics (linear resolutions of $\sim$ 2 kpc) in two representative close major-merger star-forming pairs: the spiral-elliptical pair Arp 142 and the spiral-spiral pair Arp 238. The CO in Arp 142 is widely distributed over a highly distorted disk without any nuclear concentration, and an off-centric ring-like structure is discovered in channel maps. The SFE varies significantly within Arp 142, with a starburst region (Region 1) near the eastern tip of the distorted disk showing an SFE $\sim$ 0.3 dex above the mean of the control sample of isolated galaxies, and the SFE of the main disk (Region 4) 0.43 dex lower than the mean of the control sample. In contrast, the CO emission in Arp 238 is detected only in two compact sources at the galactic centers. Compared to the control sample, Arp 238-E shows an SFE enhancement of more than 1 dex whereas Arp 238-W has an enhancement of $\sim$ 0.7 dex. We suggest that the extended CO distribution and the large SFE variation in Arp 142 are due to an expanding large-scale ring triggered by a recent high-speed head-on collision between the spiral galaxy and the elliptical galaxy, and the compact CO sources with high SFEs in Arp 238 are associated with nuclear starbursts induced by gravitational tidal torques in a low-speed coplanar interaction.

Keywords: galaxies: interactions — galaxies: evolution — galaxies: starburst — galaxies: general

1. INTRODUCTION

It is well documented that mergers can trigger enhanced star-formation in galaxies (Kennicutt et al. 1987; Sanders & Mirabel 1996). The most extreme starbursts, such as the ultraluminous infrared galaxies (ULIRGs: $L_{IR} \geq 10^{12} L_{\odot}$), are usually found in the final stage of mergers (Sanders & Mirabel 1996). Strong star-formation enhancements are also detected in earlier merger stages, particularly in major-mergers (mass ratio less than 3) during close encounters (Xu & Sulentic 1991; Nikolic et al. 2004; Ellison et al. 2010; Scudder et al. 2012). On the other hand, only a small fraction of interacting galaxies show significant star-formation enhancement (Horellou et al. 1999; Bergvall et al. 2003; Knapen & James 2009). Spitzer observations of a sample of K-band selected close major-merger pairs (Xu et al. 2010), which preferentially select early mergers during or near the first and second pericentric passages, found that only $\sim$ 25% of star-forming galaxies in the sample show strong enhancement in specific star-formation rate (sSFR = SFR/M_{star}, where SFR is the star-formation rate in $M_{\odot}$ yr^{-1} and M_{star} the stellar mass in $M_{\odot}$). Furthermore, the far-infrared (FIR) observations by Spitzer

Email: congxu@nao.cas.cn

[1] Chinese Academy of Sciences South America Center for Astronomy, National Astronomical Observatories, CAS, Beijing 100101, China
[2] National Astronomical Observatories, Chinese Academy of Sciences (NAOC), 20A Datun Road, Chaoyang District, Beijing 100101, China
[3] Dept. Física Teórica y del Cosmos, Campus de Fuentenueva, Edificio Mecenas, Universidad de Granada, E-18071 Granada
[4] Instituto Carlos I de Física Tórica y Computacional, Facultad de Ciencias, E-18071 Granada, Spain
[5] Department of Astronomy, Xiamen University, 422 Siming South Road, Xiamen 361005, China
[6] Purple Mountain Observatory & Key Laboratory for Radio Astronomy, Chinese Academy of Sciences, 10 Yuanhua Road, Nanjing 210023, China
[7] Department of Astronomy and Theoretical Physics, Lund Observatory, Box 43, SE-221 00 Lund, Sweden

and Herschel show that only star-forming galaxies in spiral-spiral (hereafter S+S) pairs have significantly enhanced sSFR, but not those in spiral-elliptical (hereafter S+E) pairs (Xu et al. 2010; Cao et al. 2016). The low fraction of paired galaxies with enhanced sSFR is often interpreted as due to the fact that strong starbursts triggered by interactions are "on" only for short periods ($\sim$ 100 Myr), while most time a merging galaxy is in the "off" phase of the starburst (DiMatteo et al. 2008). However, this interpretation cannot explain the non-enhancement of sSFR in star-forming galaxies in S+E pairs, which represent 34% of star-forming galaxies in a complete sample of K-band selected close major-merger pairs (KPAIR, Domingue et al. 2009). It was suggested (Park & Choi 2009; Hwang et al. 2011) that the lack of star-formation enhancement in S+E pairs could be due to stripping of cold gas of the spiral component by ram-pressure of the hot-gas halo surrounding the elliptical component. But this hypothesis is rejected by the results of Zuo et al. (2018) and Lisenfeld et al. (2019). Lisenfeld et al. (2019) carried out IRAM CO observations for 78 spiral galaxies selected from the H-KPAIR sample of 88 close major-merger pairs that have Herschel FIR observations (Cao et al. 2016). Combining with the GBT HI observations of Zuo et al. (2018) for pairs selected from the same H-KPAIR sample, Lisenfeld et al. (2019) found no significant difference between the total gas abundances of star-forming galaxies in S+E and in S+S pairs. Indeed, their results show that the reason for spiral galaxies in S+E pairs to have a significantly lower sSFR than their counterparts in S+S pairs (Xu et al. 2010; Cao et al. 2016) is because they have a significantly lower molecular-to-total-gas ratios ($M_{H_2}/(M_{H2}+M_{HI})$) and a lower star-formation efficiency (SFE = SFR/M_{H_2}).

In this article, we present NOEMA CO imaging observations of two representative pairs: Arp 142 (S+E) and Arp 238 (S+S). In the sample of Lisenfeld et al. (2019), the spiral component of Arp 142 (NGC 2936) has the highest SFR among galaxies in S+E pairs. Arp 238-E (UGC8335-E), a luminous

infrared galaxy (LIRG: $L_{IR} \geq 10^{11} L_\odot$), has the second highest SFR among galaxies in S+S pairs (see Table 2). Interestingly, the SFE in Arp 142 is ~ 30 times lower than that in Arp 238-E (Lisenfeld et al. 2019). With the NOEMA observations, we aim to probe the cause of the strong difference between SFEs of the two pairs, which may also shed light on the physical mechanism for the SFE difference between S+E and S+S pairs in general.

2. OBSERVATIONS

CO(1-0) was observed with the Northern Extended Millimeter Array (NOEMA) of the Institute of Radioastronomy in the Millimeter (IRAM)[8] in C and D array with 10 antennas (project W19BL). The observations were carried out under good weather conditions. For each object we made a small mosaic consisting of two overlapping regions. The receiver covers two side-bands, each with a width of 7.744 GHz. The autocorrelator PolyFix was used which has a channel width of 2 MHz (corresponding to 5.3 km s^{-1} at the frequency of our observations). The line frequency was tuned in the Upper Side Band (USB). Some basic parameters of the observations are listed in Table 1.

We reduced the data following standard procedures using the GILDAS[9] software. The data were calibrated using the IRAM package Continuum and Line Interferometer Calibration (CLIC). The standard pipeline reduction and calibration was followed to a large extent, only some poor data scans were flagged and the use of the standard flux calibrator had to be enforced in one observing run. From the resulting uv tables, a continuum table was produced combining all non-line channels in both sidebands with the tasks *uv_cont* and *uv_merge*. For the line data, a constant baseline was subtracted from the calibrated uv tables in the USB. We then reduced the table size by extracting only the channels with line emission and channels nearby. Finally, we produced uv tables with four different frequency resolutions using the task *uv_compress*: the original 2 MHz resolution, 4 MHz (corresponding to 10.6 km s^{-1}), 8 MHz (corresponding to 21.3 km s^{-1}), and 12 MHz (corresponding to 31.9 km s^{-1}).

We imaged the data with natural weighting to maximize the sensitivity. We tested different tapers in order to search for faint, extended emission, but found no evidence for it. We will therefore use the untapered data (for the beam sizes see Table 1). We tested different cleaning procedures: the robust algorithm CLEAN introduced by Högbom (1974), the variant developed by Clark (1980) and the method proposed by Steer et al. (1984, SDI) which represents a cleaning algorithm which is better adapted to extended structures. We finally selected the data cube cleaned with Högbom for the compact source Arp 238 (although no major difference was found when using the Clark algorithm), and the cube cleaned with SDI which was able to best deal with the extended emission in Arp 142 without producing artifacts. For both objects, we used the recommended loop-gain of 0.2 and truncation threshold of 0.2 of the primary beam sensitivity. The velocities in this paper are calculated using the optical convention and are relative to the Local Standard of Rest reference frame.

3. RESULTS

For both Arp 142 and Arp 238 we present integrated CO(1-0) maps, compared to Spitzer-IRAC (Xu et al. 2010) and HST images [10], in Figure 1. The total integrated CO fluxes, together with other physical parameters, are presented in Table 2. As shown in Figure 1, the CO in Arp 142 is widely distributed within a highly distorted disk of NGC 2936. While the CO traces quite well the star-formation as traced by Spitzer (the red areas in Figure 1b, which also coincide with the dust lanes in the Hubble images), there is no CO concentration in the nucleus (Region 2 in Figure 1b). The total CO flux measured in the NOEMA map of Arp 142 (Table 2) is a factor of 1.35 higher than that detected by IRAM-30m (175.3 ± 2.8 Jy km s^{-1}, Lisenfeld et al. 2019), because the NOEMA measurement covers a significantly larger area than the IRAM beam (FWHM=22$''$). Assuming the standard conversion factor $\alpha_{CO} = 3.2$ M$_\odot$K^{-1}km^{-1}s pc^2 (Bolatto et al. 2013), the total molecular gas mass of Arp 142 is $M_{mol} = 10^{10.29 \pm 0.02}$ M$_\odot$. This is about a factor of 2 higher than that of Bothwell et al. (2014) based on a CO(2-1) observation of APEX, which has a beam (27$''$) significantly smaller than the size of the CO emission (Figure 1a). On the other hand, the M_{mol} is 0.39 dex lower than that estimated by Lisenfeld et al. (2019), suggesting that the large aperture correction ($f_{aper} = 3.16$) adopted by Lisenfeld et al. (2019) might have been over-estimated.

For Arp 238, CO is detected only in two compact sources at the centers of the two galaxies. Both sources can be fitted well with elliptical 2-D Gaussian functions of FWHM = $4.4'' \times 3.8''$ with P.A. = 80° (Arp 238-E) and and FWHM = $4.4'' \times 3.3''$ with P.A. = 90° (Arp 238-W), respectively. Neglecting the small difference between the P.A. of each source and that of the beam (P.A. = 88°, Table 1), the intrinsic sizes of these sources after the deconvolution are $2.8'' \times 2.3''$ (Arp 238-E) and $2.8'' \times 1.3''$ (Arp 238-W), respectively. These are smaller than the NOEMA beam size (see Table 1), and slightly larger than the sizes of radio continuum sources ($\sim 1'' - 2''$) detected in the high resolution VLA maps of Condon et al. (1991). No diffuse CO is detected in Arp 238. Compared to their CO fluxes measured by IRAM-30m (51.8 ± 3.4 Jy km s^{-1} and 37.0 ± 3.3 Jy km s^{-1}), the NOEMA observations missed 9% and 26% of the CO emissions of Arp 238-E and Arp 238-W, respectively. The missed emissions are most likely associated with diffuse gas in the disks and/or tidal tails. The continuum was detected only at the nucleus of Arp 238-E as a point source. No continuum emission was detected in Arp 142, nor in Arp 238-W.

Figure 2 shows the channel maps of Arp 142. Interestingly, there appears to be an off-centric ring-like structure in the channel maps of v < 7000 km s^{-1}, most clearly visible in the channel of v = 6893 km s^{-1}. It seems to grow in size from v = 6765 km s^{-1} to v = 6957 km s^{-1}. This could be an expanding cone-like structure in 3-D with the top of the cone moving toward the observer (i.e. blue-shifted), which is also the direction of the motion of the elliptical companion (z = 0.02265, corresponding to v = 6795 km s^{-1}). Notably, most CO of v > 7000 km s^{-1} is in the north, and the channel maps are consistent with a highly distorted rotating disk.

The spectrum of the integrated emission of Arp 142 is pre-

---

[10] The HST data are based observations made with the NASA/ESA Hubble Space Telescope, and obtained from the Hubble Legacy Archive, which is a collaboration between the Space Telescope Science Institute (STScI/NANA), the Space Telescope European Coordinating Facility (ST-ECF/ESA) and the Canadian Astronomy Data Centre (CAD/NRC/CSA).

Table 1
Summary of the CO(1-0) observations and properties of the final data cube.

	Arp 142	**Arp 238**
Observation details:		
Dates	April 12-15, 2020	May 8-24, 2020
Total observing time	4.4 hours	3.7 hours
Center position of mosaic	RA: 09:37:43.90	RA: 13:15:32.77
	DEC: 02:45:26.0	DEC: 62:07:37.6
Offsets of mosaic pointings (RA, DEC)	$(7.5'', 8.0'')$	$(10.0'', -5.0'')$
	$(-7.5'', -8.0'')$	$(-10.0'', 5.0'')$
Observed central frequency	112.644262 GHz	111.82685 GHz
Flux calibrator	LKHA101	MWC349
Bandpass calibrator	3C84 ; J0854+2006	3C273; J1751+0939
Phase calibrator	J0930+0034; J0909+0121	J1302+5748 ; J1302+6902
Properties of final data cubes:		
Beam size of cleaned image	$4.28'' \times 3.44''$	$3.36'' \times 3.02''$
Position angle of beam	$-4°$	$88°$
Mean noise of cleaned image	1.14 mJy/beam	0.73 mJy/beam
(frequency resolution of 12 MHz)		

Table 2
NOEMA results and other physical parameters of Arp 142 and Arp 238

	NGC 2936 (in Arp 142)	**Arp 238-E**	**Arp 238-W**	**reference**
$I_{CO(1-0)}$ [Jy km s^{-1}] [a]	237.4 ± 12.4	47.0 ± 2.4	27.5 ± 1.4	this work
$f_{2.6mm}$ [mJy]	......	3.9 ± 1.0	......	this work
optical redshift	0.02331	0.03078	0.03080	Domingue et al. (2009)
luminosity distance [Mpc]	104.0	134.1	134.1	Cao et al. (2016)
kpc per arcsec	0.49	0.63	0.63	
$\log(M_{mol})$ [M$_\odot$] [b]	10.29 ± 0.02	9.84 ± 0.02 [c]	9.70 ± 0.02 [d]	this work
$\log(M_{HI})$ [M$_\odot$]	9.70 ± 0.05	9.70 ± 0.07 [e]		Zuo et al. (2018), Huchtmeier & Richter (1989)
$\log(M_{gas})$ [M$_\odot$] [f]	10.39 ± 0.02	10.23 ± 0.04		this work
$\log(M_{dust})$ [M$_\odot$]	8.37 ± 0.09	7.81 ± 0.09	7.80 ± 0.09	Cao et al. (2016)
M_{dust}/M_{gas}	0.0095 ± 0.0024	0.0076 ± 0.0017		this work
$\log(M_{star})$ [M$_\odot$]	11.16	10.80	10.62	Cao et al. (2016)
$\log(L_{IR})$ [L$_\odot$]	10.96	11.71	10.84	Cao et al. (2016)
SFR [M$_\odot$ yr^{-1}] [g]	9.83	55.30	7.59	Cao et al. (2016)

Notes: [a] Each flux error is estimated as the sum of the rms error and a 5% error including uncertainties of the background subtraction, aperture setting, and the calibration. [b] The standard conversion factor $\alpha_{CO} = 3.2$ M$_\odot$K^{-1}km^{-1}s pc^2 (Bolatto et al. 2013) is adopted. [c] A missing flux correction factor of 1.10, estimated from the comparison with the IRAM single dish result of Lisenfeld et al. (2019), is applied to the NOEMA CO flux. [d] The missing flux correction factor is 1.35. [e] The HI observation includes both Arp 238-E and Arp 238-W. [f] The total cold gas mass $M_{gas} = M_{mol} + M_{HI}$. [g] Assuming SFR (M$_\odot$ yr^{-1}) = $1.086 \times 10^{-10} \times (L_{IR}/L_\odot)$.

sented in Figure 3. It shows an asymmetric double-horn shape, representing a distorted disk. As shown in channel maps (Figure 2), the ring-like structure resides in the blue peak which has a FWHM of ~ 300 km s^{-1}, significantly broader than the red peak (FWHM ~ 100 km s^{-1}). The total spectrum is very wide with a full width at zero intensity (FWZI) of ~ 1000 km s^{-1}, similar to that of Arp 118 which is a LIRG and a ring galaxy with extremely high CO luminisity (Gao et al. 1997).

Because neither of the two galaxies in Arp 238 is well resolved, we show only the spectra of their integrated emissions in Figure 4. Both sources have broad (FWHM~ 400 km s^{-1}) and multi-peak line profiles, suggesting complex kinematics within them. This is consistent with the strong interaction between them revealed by the long tidal tails shown in optical maps, and with their high SFR which can cause strong turbulence and feedbacks.

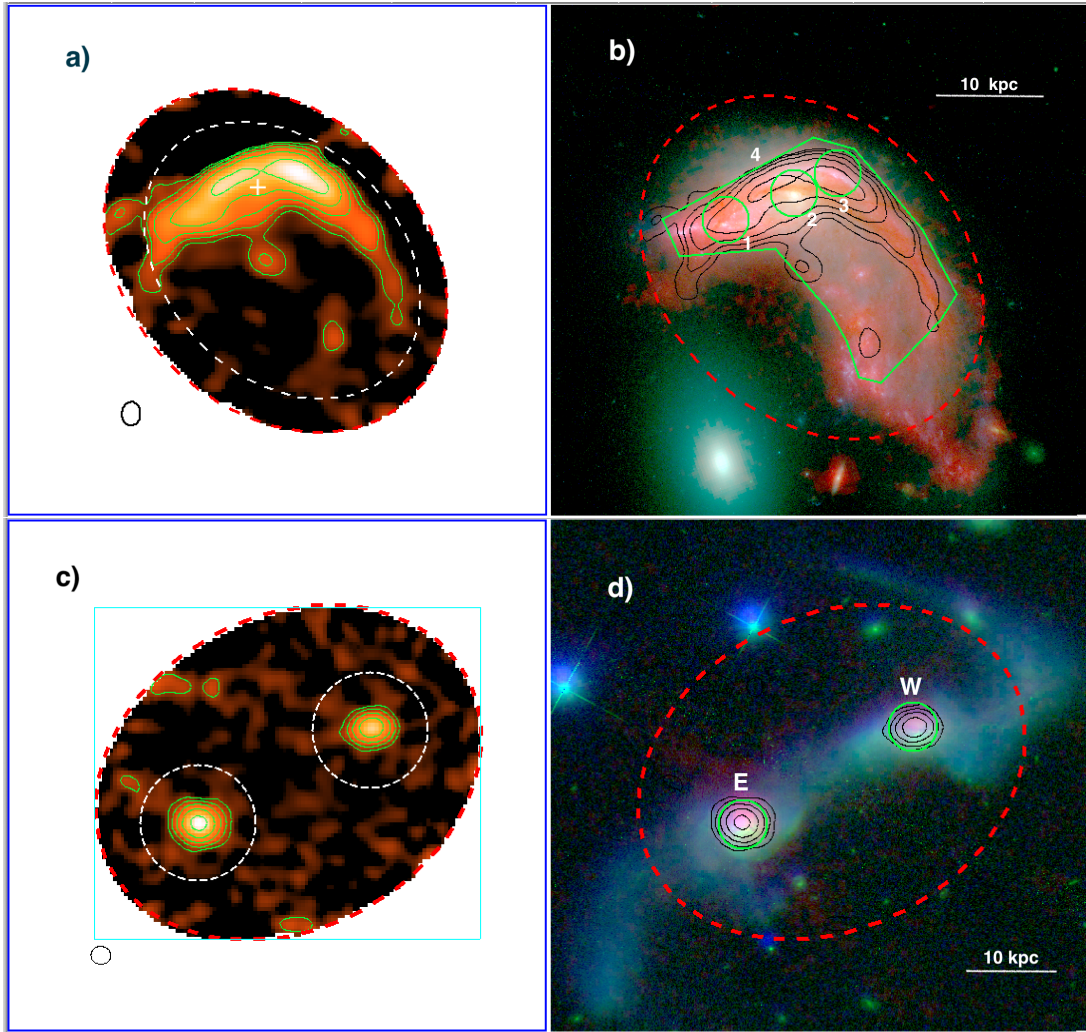In order to investigate how the SFE varies within the two

Figure 1. *Panel a)*: Integrated CO(1-0) map of Arp 142. The contour levels are at 1, 2, 4, 8, 16 Jy km s^{-1} beam^{-1}. The noise of the map is non-uniform, varying between 0.3 Jy km s^{-1} beam^{-1} (inner region) and 0.5 Jy km s^{-1} beam^{-1} (outer region). The small black ellipse in the lower-left corner of the panel represents the beam, which has the FWHM of 4.28$''\times$3.44$''$, corresponding to a physical scale of 2.1 kpc $\times$ 1.7 kpc. The white dashed ellipse (size=47.1$''\times$42.6$''$) outlines the aperture for the measurement of the total CO flux. The white plus sign marks the nucleus. *Panel b)*: Optical-IR three-color plot (blue: HST-F475W, green: HST-F814W, red: IRAC-8.0μm) of Arp 142, overlaid by the same CO contours (black) as in Panel a). The four regions (with green boundaries) are: Region 1 - off-nucleus starburst region (Mora et al. 2019), Region 2 - nuclear region, Region 3 - CO peak region, Region 4 - main disk. The red dashed ellipse outlines the field of view of NOEMA observation. *Panel c)*: Integrated CO(1-0) map of Arp 238. The small black ellipse in the lower-left corner of the panel represents the beam (3.36$''\times$3.02$''$, corresponding to a physical scale of 2.1 kpc $\times$ 1.9 kpc). The contour levels are at 1, 2, 4, 8, 16 Jy km s^{-1} beam^{-1}. The noise of the map is in the range of 0.2 Jy km s^{-1} beam^{-1} (inner region) and 0.5 Jy km s^{-1} beam^{-1} (outer region). The white dashed circles (with $D = 20''$) outline the apertures for the measurements of the total CO fluxes of the two galaxies. *Panel d)*: Optical-IR three-color plot (blue: HST-F435W, green: HST-F814W, red: IRAC-8.0μm) of Arp 238, overlaid by the same CO contours (black) as in Panel c). The two green circles mark the two central regions around the two nuclei. The red dashed ellipse outlines the field of view of NOEMA observations.

pairs, we inspect several regions in Arp 142 (defined in Figure 1b) and the two central regions in Arp 238 (Figure 1d). The results are listed in Table 3. For Arp 142, the main disk (Region 4) has a rather low SFE, 0.43 dex lower than the mean of AMIGA control sample of Lisenfeld et al. (2019) which is $\log(\text{SFE}/\text{yr}^{-1}) = -9.07 \pm 0.05$. Interestingly, there is a significant variation of SFE within Arp 142. The CO-peak region (Region 3) has a similarly low log(SFE) as that of Region 4, and log(SFE) of the nuclear region (Regino 2) is comparable to the mean of the control sample. On the other hand, the starburst region (Region 1) near the eastern tip of the distorted disk has an SFE more than 0.7 dex higher than that of Region 3, showing a moderate SFE enhancement (~ 0.3 dex) compared to the control sample. However, only $\sim 10\%$ of molecular gas in Arp 142 is found in Region 1, the majority of the remaining gas is likely to have relatively low SFE, as

suggested by the result of Region 4. In contrast, the two central regions in Arp 238 dominate the total M_{mol} in Arp 238, and both have very high SFEs. Compared to the control sample, Arp 238-E shows an SFE enhancement of more than 1 dex whereas Arp 238-W has an enhancement of ~ 0.7 dex.

In Figure 5 the SFR surface densities (Σ_{SFR}) of regions in Table 3 are plotted against the surface densities of molecular gas (Σ_{mol}). They scatter around the standard Kennicutt-Schmidt relation (hereafter K-S relation; Kennicutt 1998), with most of regions in Arp 142 found below the K-S relation and the two central regions in Arp 238 high above it. It is worth pointing out that the CO emission in Arp 238-E and Arp 238-W is not resolved, and the estimated intrinsic sizes of the two sources are much smaller than that of the two central regions. Also, observations of various SFR indicators in the radio continuum (Condon et al. 1991), in 8μm

Table 3
Properties of Regions of Interest in Arp 142 and Arp 238 [a]

Name	RA & Dec (J2000)	size[b] [kpc]	$I_{CO(1-0)}$ [Jy km s^{-1}]	$\log(M_{mol})$[c] [M$_\odot$]	$\log(L_{8\mu m,dust})$[d] [L$_\odot$]	$\log(SFR)$[e] [M$_\odot$ yr^{-1}]	$\log(SFE$[f]) [yr^{-1}]
Arp 142:							
Region 1[g]	09:37:44.97 +02:45:34.4	4.2	31.71± 0.86	9.42	9.98	0.68	-8.74
Region 2[h]	09:37:44.14 +02:45:39.3	4.2	40.17± 0.97	9.52	9.64	0.34	-9.18
Region 3[i]	09:37:43.61 +02:45:43.0	4.2	49.20± 1.07	9.61	9.43	0.12	-9.49
Region 4[j]	09:37:43.92 +02:45:25.8	18.0	246.6± 2.40	10.31	10.11	0.81	-9.50
Arp 238:							
E[k]	13:15:34.93 +62:07:29.1	5.4	38.43± 1.15	9.72	11.00	1.69	-8.03
W[l]	13:15:30.70 +62:07:45.2	5.4	22.68± 0.90	9.49	10.42	1.11	-8.38

Notes: [a] See Panels b) and d) of Figure 1 for definitions of the regions. [b] For circular regions: size = diameter; for irregular regions: size = $2 \times \sqrt{area/\pi}$. [c] Assuming α_{CO} = 3.2 M$_\odot$K^{-1}km^{-1}s pc^2 (Bolatto et al. 2013). [d] Derived from f$_{8\mu m,dust}$ = f$_{8\mu m}$ − 0.232 × f$_{3.6\mu m}$, where f$_{8\mu m}$ and f$_{3.6\mu m}$ are flux densities in units of Jy (Helou et al. 2004). These are measured after convolving the original Spitzer-IRAC 8μm image (beam-size (FWHM) =2.0$''$) and 3.6μm image (beam-size (FWHM) =1.8$''$) to the NOEMA resolutions. [e] Assuming L$_{IR}$ = 4.55 × L$_{8\mu m,dust}$ (Shivaei et al. 2017), and SFR (M$_\odot$ yr^{-1}) = 1.086 × 10^{-10} × (L$_{IR}$/L$_\odot$) (Cao et al. 2016). [f] SFE = SFR/M$_{H_2}$. [g] Off-nucleus starburst region (Mora et al. 2019). [h] Nuclear region of NGC 2936. [i] Region of the peak of the CO(1-0) emission. [j] Main disk of NGC 2936. The size of this irregular region is defined to be equal to $2 \times \sqrt{area/\pi}$. [k] Central region of Arp 238-E. [l] Central region of Arp 238-W.

Spitzer-IRAC band (Xu et al. 2010), and in Hα line emission (Hattori et al. 2004) all show the dominance of two nuclear sources over the entire pair. The high resolution 8.44 GHz VLA maps (beam = 0.25$''$) of Condon et al. (1991) show that the emission regions associated with Arp 238-E and Arp 238-W have sizes of ∼ 2$''$ and ∼ 1$''$, respectively. These are even smaller than the estimated intrinsic sizes of the CO emission regions (2.8$'' \times$2.3$''$ for Arp 238-E, 2.8$'' \times$1.3$''$ for Arp 238-W). Assuming that both CO and 8μm emissions in Arp 238-E are from an elliptical region of size 2.8$'' \times$2.3$''$ and those in Arp 238-W from a region of size 2.8$'' \times$1.3$''$, we raise both Σ_{SFR} and Σ_{mol} of Arp 238-E by a factor of 11.5 and Σ_{SFR} and Σ_{mol} of Arp 238-W by a factor of 20.3. This moves the data points representing the two central regions to the upper-right part of the K-S plot and, because of the non-linearity of the K-S relation (power = 1.4), much closer to the line of the K-S relation.

There is a large uncertainty for the conversion factor α_{CO}, in particular for (U)LIRGs (Bolatto et al. 2013; Downes & Solomon 1998). We compare the molecular gas mass estimated using the adopted α_{CO} with the HI mass (Zuo et al. 2018) and dust mass (Cao et al. 2016) for Arp 142 and Arp 238, in order to constrain the effect of this uncertainty to our results. As shown Table 2, the dust-to-gas ratios of the two pairs are 0.0095 ± 0.0024 and 0.0076 ± 0.0017, both consistent with the value (∼ 0.007) of Draine et al. (2007) obtained for local spiral galaxies. This suggests that globally our results are not significantly affected by the uncertainty of α_{CO}. It is worth noting that Lisenfeld et al. (2019) made an in-depth discussion on the applicability of the standard conversion factor to a sample of close major-merger pairs, to which both Arp 142 and Arp 238 belong, and concluded that their results on molecular mass derived using α_{CO} = 3.2 M$_\odot$K^{-1}km^{-1}s pc^2 are robust. Nevertheless, conservatively, we put an error bar of a factor of 3 for Σ_{mol} (Renaud et al. 2019) in Figure 5, applicable to all data points in the plot. Also plotted is an error

bar of a factor of 2 for Σ_{SFR} (dominated by systematic uncertainties in the L$_{8\mu m,dust}$-to-SFR conversion).

4. DISCUSSION

Given the peculiar optical morphology of Arp 142 and Arp 238, it is likely that both pairs have undergone strong interactions recently, and their very different molecular gas distributions and SFEs found in NOEMA observations are due to differences in their interactions. The dynamic histories of both Arp 142 and Arp 238 were simulated by Holincheck et al. (2016) using a simple three-body simulation code, and their best models found that both pairs have undergone close encounters recently: For Arp 142, the pericentric passage has r$_{min}$ = 8.95 ± 1.14 kpc and occurred t$_{min}$ = 78.0 ± 6.3 Myr ago, whereas for Arp 238 r$_{min}$ = 12.54 ± 2.95 kpc and t$_{min}$ = 58.9 ± 13.1 Myr. On the other hand, the two interacting systems have diagonally different orbital orientations: while the interaction is coplanar for both galaxies in Arp 238, it is nearly perpendicular for the spiral galaxy in Arp 142. Also, the radial velocity difference between the two galaxies in Arp 142 is 201 km s^{-1}, significantly higher than that of Arp 238 which is only 6 km s^{-1}. Mora et al. (2019) found a best-match model for Arp 142 in the suite of more sophisticated Galmer SPH simulations (DiMatteo et al. 2008; Chilingarian et al. 2010), which agrees very well with that of Holincheck et al. (2016), with r$_{min}$ = 8 kpc, v$_{min}$ = 300 km s^{-1}, t$_{min}$ = 52 ± 25 Myr, and the disk of the spiral galaxy perpendicular to the orbit plane.

Thus, simulation results indicate that Arp 142 and Arp 238 have gone through very different types of interactions: the former a high-speed (∼ 300 km s^{-1}) head-on collision between the disk and the elliptical companion, and the latter a low-speed coplanar interaction between two spiral galaxies. Both observations and simulations (Theys & Spiegel 1977; Appleton & Struck-Marcell 1987, 1996) have shown that off-centric high-speed head-on collision produces ring-like den-
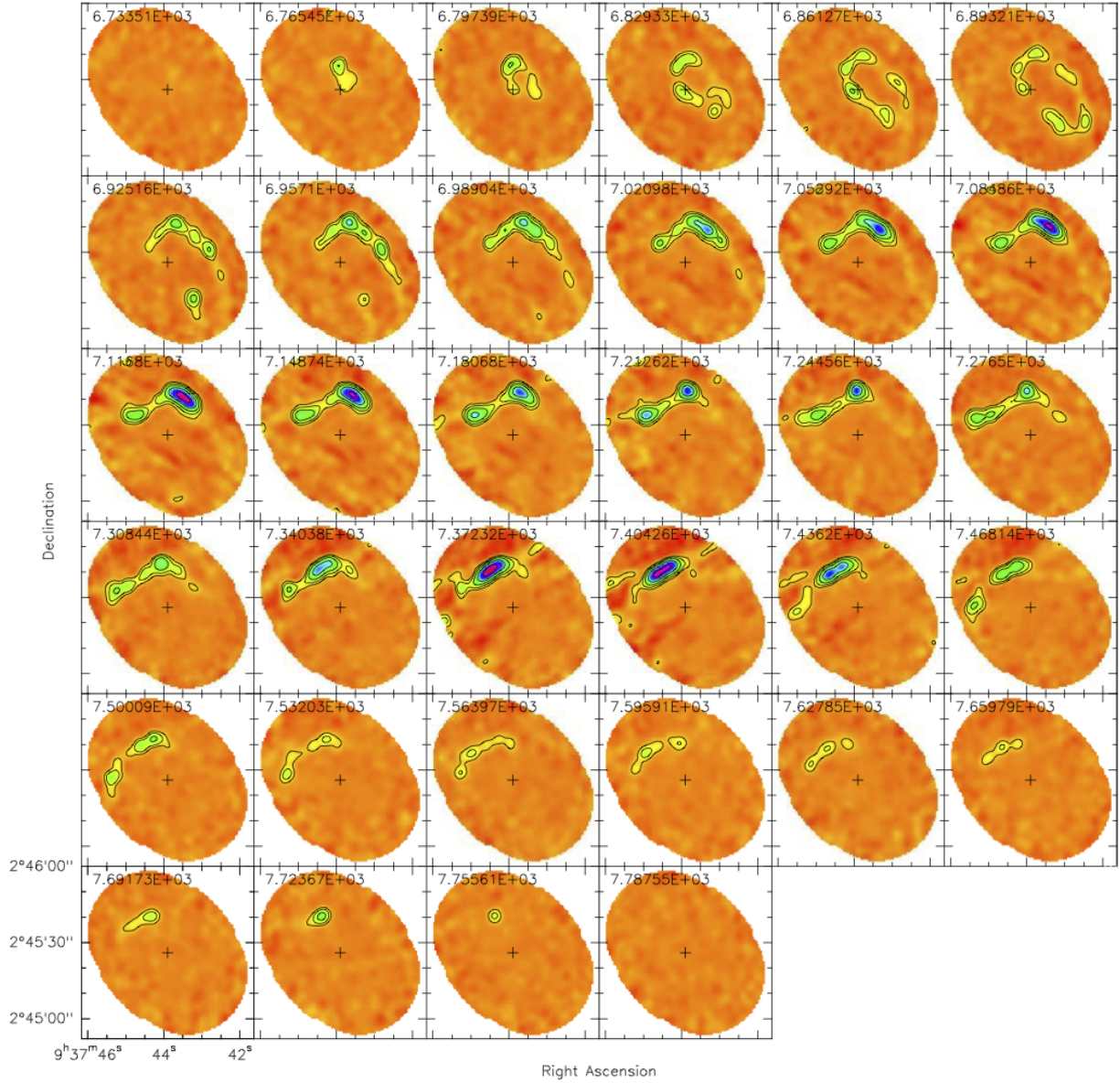
Figure 2. CO(1-0) channel maps of Arp 142. The bandwidth of the channels is 31.9 km s^{-1}. The central velocity of each channel is marked in the corresponding map. The contour levels are at 6.9, 13.8, 27.6, 55.2, and 110.4 mJy beam^{-1}.

sity waves expanding through both stellar and gaseous disks, and pushing gas in the central region to the outer disk. This scenario is consistent with the NOEMA data of Arp 142. Meanwhile, shocks and turbulence associated with the ring can either compress gas clouds and trigger starbursts similar to that in Arp 142 (Gao et al. 1997; Lamb et al. 1998; Higdon et al. 2011; Renaud et al. 2018), or inject kinematic energy into clouds and stabilize them against collapse (Alatalo et al. 2014; Guillard et al. 2012). Whether this can explain the large variation of the SFE in Arp 142 will be the subject of a follow-up study of the kinematics and its relation to SFE in Arp 142, via a high resolution hydrodynamic simulation (Renaud et al. in preparation).

On the other hand, the very high SFEs of Arp238-E and Arp 238-W are apparently related to the compactness of the starbursts in their nuclei, which have Σ_{mol} approaching those of ULIRGs (Scoville et al. 1991). This can be explained by simulations of Barnes & Hernquist (1996) and Hopkins et al.

(2009), which predicted that gravitational tidal torques in low-speed coplanar interactions can trigger strong gas inflows that lead to nuclear gas concentrations and nuclear starbursts.

Does the contrast between Arp 142 and Arp 238 represents a common difference between S+E and S+S pairs? Namely, do more S+E pairs have high-speed and high-inclination interactions while low-speed coplanar interactions are more common in S+S pairs? A definite answer to this question can only be obtained through dynamic simulations of a complete pair sample, which is beyond the scope this paper. However, some hints can be found in the following statistics of the H-KPAIR sample (Cao et al. 2016): For S+E pairs in H-KPAIR, the average radial velocity difference between pair members is 215.7 ± 20.4 km s^{-1}, higher than that for S+S which is 165.9 ± 18.2 km s^{-1}. Also, for S+E pairs and S+S pairs, the means of the number of galaxies of $M_r \leq -19.5$ found within 1 Mpc projected radius from the pair center and with redshift
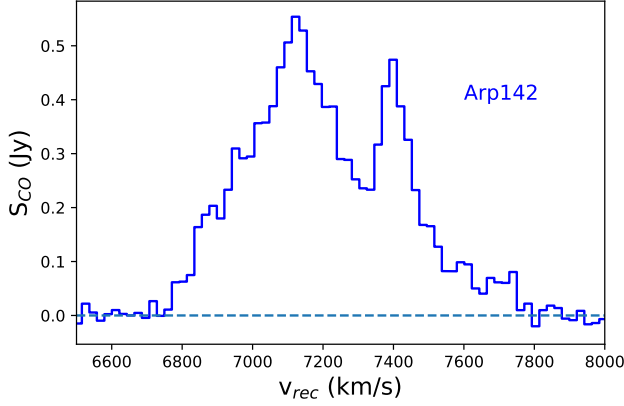
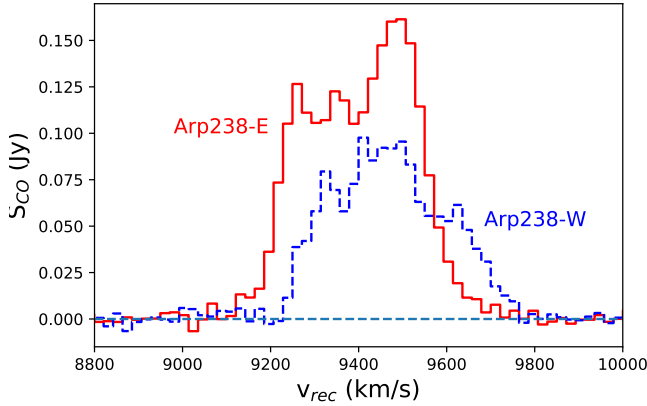**Figure 3.** CO spectrum of integrated emission of Arp 142 (within the white ellipse shown in Fig. 1a).

Figure 4. CO Spectra of **integrated** emissions of two galaxies in Arp 238 (within the white circles shown in Fig. 1c).

differences (compared to that of the pair) < 500 km s^{-1} are 5.14 ± 0.59, and 3.81 ± 0.35, respectively. This indicates that, compared to S+S pairs, S+E pairs are in higher local density environment and therefore more likely found in groups or clusters. While isolated pairs formed in IGM filaments may preferentially have coplanar orbits, pairs in groups/clusters are likely to have significantly disturbed orbits that are more randomly oriented, as suggested by the results of Dubois et al. (2014). Indeed, Arp 142 itself is in a group with 6 members brighter than $M_r = -19.5$, and NGC 2936 is the first-ranked member of the group (Yang et al. 2007). It is worth noting that Elagali et al. (2018) found, in an investigation of results of EAGLE simulations, that ring galaxies triggered by recent high-inclination collisions are more likely found in massive groups, and they tend to have low SFEs. These results favor the hypothesis that S+E pairs are more likely to have high-speed and high-inclination interactions and S+S pairs low-speed coplanar interactions, which may result in a lower chance for S+E pairs to have high SFE nuclear starbursts compared to S+S pairs.

5. SUMMARY AND CONCLUSIONS

Previous observations of the SFR (Cao et al. 2016) and the molecular (Lisenfeld et al. 2019) and atomic (Zuo et al. 2018) gas content of the H-KPAIR sample have shown pronounced differences between S+E and S+S pairs: The sSFR
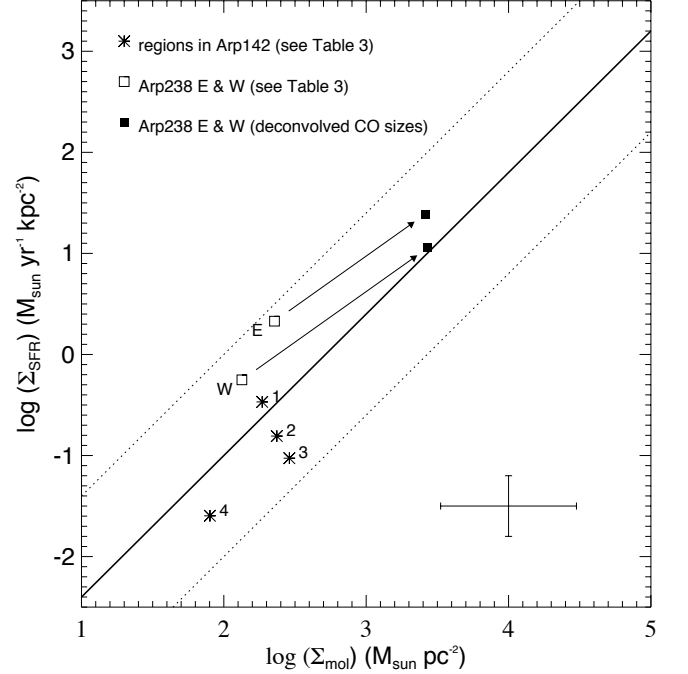

Figure 5. Kennicutt-Schmidt (K-S) plot of regions in Arp 142 and Arp 238 (see Table 3 for their definitions). For the two central regions in Arp 238 (E and W), the black filled squares show the estimated Σ_{SFR} and Σ_{mol} values when the sizes in Table 3 are replaced by the deconvolved sizes of the corresponding CO sources. Black solid line shows the K-S relation (Kennicutt 1998) converted to the Kroupa IMF, and the two dotted lines mark the limits of 10 times deviation. The large black plus sign in the bottom right corner illustrates error bars of Σ_{SFR} (a factor of 2) and of Σ_{mol} (a factor of 3), dominated by systematic uncertainties in the $L_{8um,dust}$-to-SFR and L_{CO}-to-M_{mol} conversions, respectively.

is only enhanced in S+S pairs, and there is a significant difference between the SFEs of S+E and S+S pairs (Lisenfeld et al. 2019). In order to probe the physical mechanism for these differences, we carried out NOEMA imaging observations of CO(1-0) line emission in two representative pairs: the S+E pair Arp 142 and the S+S pair Arp 238. In the sample of Lisenfeld et al. (2019), the spiral component of Arp 142 has the highest SFR among galaxies in S+E pairs and Arp 238-E (a LIRG) the second highest SFR among galaxies in S+S pairs, whereas the SFE of the former is about 30 times lower than that of the latter.

The NOEMA observations, with a linear resolution of about 2 kpc, gave the following results:

- The CO emission in Arp 142 is widely distributed over a highly distorted disk of the spiral galaxy (NGC 2936) without any nuclear concentration, and an off-centric ring-like structure is discovered in channel maps.

- There is a significant variation of the SFE within Arp 142. The starburst region (Region 1) near the eastern tip of the distorted disk has an SFE more than 0.7 dex higher than that of the CO-peak region (Region 3) and shows a moderate SFE enhancement (~ 0.3 dex) compared to the mean of the AMIGA control sample of isolated galaxies (Lisenfeld et al. 2019).

- Only $\sim 10\%$ of the molecular gas in Arp 142 is found in the starburst region, whereas the majority of the remaining gas has relatively low SFE as suggested by the

result for the main disk (Region 4) which has an SFE 0.43 dex lower than the mean of control sample.

- In Arp 238, CO is detected only in two compact sources at the two galactic centers.

- The two central regions in Arp 238 dominate the total M_{mol} in Arp 238, and both have very high SFEs. Compared to the control sample, Arp 238-E shows an SFE enhancement of more than 1 dex whereas Arp 238-W has an enhancement of ~ 0.7 dex.

The differences between these two merger pairs are most likely due to different orbital parameters of the encounters: Simulations in the literature (Holincheck et al. 2016; Mora et al. 2019) have found that Arp 142 has undergone a high-speed off-centric head-on collision while the Arp 238 has gone through a low-speed coplanar interaction. The extended CO distribution and large SFE variation in Arp 142 are most likely related to the shocks and turbulence associated with an expanding large-scale ring triggered by the head-on collision. On the other hand, the very high SFEs of Arp238-E and Arp 238-W are related to the compactness of the starbursts in their nuclei which have very high Σ_{mol}. As predicted by simulations (Barnes & Hernquist 1996; Hopkins et al. 2009), gravitational tidal torques in low-speed coplanar interactions can trigger strong gas inflows that lead to nuclear gas concentrations and nuclear starbursts.

These differences in orbits might be typical for S+S and S+E pairs in general. Statistics for the H-KPAIR sample indicate that on average S+E pairs have a higher radial velocity difference and are more likely found in groups or clusters compared to S+S pairs. Since isolated pairs formed in IGM filaments may preferentially have coplanar orbits (Dubois et al. 2014) and pairs in groups/clusters are expected to have significantly disturbed orbits that are more randomly oriented, we propose the following hypothesis in analog to the NOEMA results for Arp 142 and Arp 238: S+E pairs are more likely to have high-speed and high-inclination interactions and S+S pairs low-speed coplanar interactions, which may result in a lower chance for S+E pairs to have high SFE nuclear starbursts compared to S+S pairs.

REFERENCES

Alatalo, K., Appleton, P. N., Lisenfeld, U., Bitsakis, T., Guillard, P., Charmandaris, V., Cluver, M., Dopita, M. A., Freeland, E., Jarrett, T., Kewley, L. J., Ogle, P. M., Rasmussen, J., Rich, J. A., Verdes-Montenegro, L., Xu, C. K., & Yun, M. 2014, ApJ, 795, 159
Appleton, P. N. & Struck-Marcell, C. 1987, ApJ, 318, 103
—. 1996, Fund. Cosmic Phys., 16, 111
Barnes, J. & Hernquist, L. 1996, ApJ, 471, 115
Bergvall, N., Laurikainen, E., & Aalto, S. 2003, A&A, 405, 31
Bolatto, A. D., Wolfire, M., & Leroy, A. K. 2013, ARA&A, 51, 207
Bothwell, M. S., Wagg, J., Cicone, C., Maiolino, R., Møller, P., Aravena, M., De Breuck, C., Peng, Y., Espada, D., Hodge, J. A., Impellizzeri, C. M. V., Martín, S., Riechers, D., & Walter, F. 2014, MNRAS, 445, 2599
Cao, C., Xu, C. K., Domingue, D., et al. 2016, ApJS, 222, 16
Chilingarian, I. V., Di Matteo, P., Combes, F., Melchior, A. L., & Semelin, B. 2010, A&A, 518, A61
Clark, B. G. 1980, A&A, 89, 377
Condon, J. J., Huang, Z.-P., Yin, Q.-F., & Thuan, T. 1991, ApJ, 378, 65
DiMatteo, P., Bournaud, F., Martig, M., Combes, F., Melchior, A. L., & Semelin, B. 2008, A&A, 492, 31
Domingue, D. L., Xu, C. K., et al. 2009, ApJ, 695, 1559
Downes, D. & Solomon, P. M. 1998, ApJ, 507, 615
Draine, B. T., Dale, D. A., Bendo, G., et al. 2007, ApJ, 663, 866
Dubois, Y., Pichon, C., Welker, C., Le Borgne, D., Devriendt, J., Laigle, C., Codis, S., Pogosyan, D., Arnouts, S., Benabed, K., Bertin, E., Blaizot, J., Bouchet, F., Cardoso, J. F., Colombi, S., de Lapparent, V., Desjacques, V., Gavazzi, R., Kassin, S., Kimm, T., McCracken, H., Milliard, B., Peirani, S., Prunet, S., Rouberol, S., Silk, J., Slyz, A., Sousbie, T., Teyssier, R., Tresse, L., Treyer, M., Vibert, D., & Volonteri, M. 2014, MNRAS, 444, 1453
Elagali, A., Lagos, C. D. P., Wong, O. I., Staveley-Smith, L., Trayford, J. W., Schaller, M., Yuan, T., & Abadi, M. G. 2018, MNRAS, 481, 2951
Ellison, S. L., Patton, D. R., Simard, L., et al. 2010, MNRAS, 407, 1514
Gao, Y., Solomon, P. M., Downes, D., & Radford, S. J. E. 1997, ApJ, 481, L35
Guillard, P., Boulanger, F., Pineau des Forêts, G., Falgarone, E., Gusdorf, A., Cluver, M. E., Appleton, P. N., Lisenfeld, U., Duc, P.-A., Ogle, P. M., & Xu, C. K. 2012, ApJ, 749, 158
Hattori, T., Yoshida, M., Ohtani, H., Sugai, H., Ishigaki, T., Sasaki, M., Hayashi, T., Ozaki, S., Ishii, M., & Kawai, A. 2004, AJ, 127, 736
Helou, G., Roussel, H., Appleton, P., Frayer, D., Stolovy, S., Storrie-Lombardi, L., Hurt, R., Lowrance, P., Makovoz, D., Masci, F., Surace, J., Gordon, K. D., Alonso-Herrero, A., Engelbracht, C. W., Misselt, K., Rieke, G., Rieke, M., Willner, S. P., Pahre, M., Ashby, M. L. N., Fazio, G. G., & Smith, H. A. 2004, ApJS, 154, 253
Higdon, J. L., Higdon, S. J. U., & Rand, R. J. 2011, ApJ, 739, 97
Högbom, J. A. 1974, A&AS, 15, 417
Holincheck, A. J., Wallin, J. F., Borne, K., Fortson, L., Lintott, C., Smith, A. M., Bamford, S., Keel, W. C., & Parrish, M. 2016, MNRAS, 459, 720
Hopkins, P. F., Cox, T. J., Younger, J. D., & Hernquist, L. 2009, ApJ, 691, 1168
Horellou, C., Booth, R. S., & Karlsson, B. 1999, Ap&SS, 269, 629
Huchtmeier, W. K. & Richter, O. G. 1989, A General Catalog of HI Observations of Galaxies. The Reference Catalog.
Hwang, H. S., Elbaz, D., Dickinson, M., et al. 2011, A&A, 535, 60
Kennicutt, R. C. 1998, ApJ, 498, 541
Kennicutt, R. C., Keel, W., van der Hulst, J., et al. 1987, AJ, 93, 1001
Knapen, J. H. & James, P. 2009, ApJ, 698, 1437
Lamb, S. A., Hearn, N. C., & Gao, Y. 1998, ApJ, 499, L153
Lisenfeld, U., Xu, C. K., Gao, Y., Domingue, D. L., Cao, C., Yun, M. S., & Zuo, P. 2019, A&A, 627, A107
Mora, M. D., Torres-Flores, S., Firpo, V., Hernandez-Jimenez, J. A., Urrutia-Viscarra, F., & Mendes de Oliveira, C. 2019, MNRAS, 488, 830
Nikolic, B., Cullen, H., & Alexander, P. 2004, MNRAS, 355, 874
Park, C. & Choi, Y.-Y. 2009, ApJ, 691, 1828
Renaud, F., Athanassoula, E., Amram, P., Bosma, A., Bournaud, F., Duc, P. A., Epinat, B., Fensch, J., Kraljic, K., Perret, V., & Struck, C. 2018, MNRAS, 473, 585
Renaud, F., Bournaud, F., Agertz, O., Kraljic, K., Schinnerer, E., Bolatto, A., Daddi, E., & Hughes, A. 2019, A&A, 625, A65
Sanders, D. B. & Mirabel, I. F. 1996, ARA&A, 34, 749

Scoville, N. Z., Sargent, A. I., Sanders, D. B., & Soifer, B. T. 1991, ApJ, 366, L5

Scudder, J. M., Ellison, S. L., Torrey, P., et al. 2012, MNRAS, 426, 549

Shivaei, I., Reddy, N. A., Shapley, A. E., Siana, B., Kriek, M., Mobasher, B., Coil, A. L., Freeman, W. R., Sanders, R. L., Price, S. H., Azadi, M., & Zick, T. 2017, ApJ, 837, 157

Steer, D. G., Dewdney, P. E., & Ito, M. R. 1984, A&A, 137, 159

Theys, J. C. & Spiegel, E. A. 1977, ApJ, 212, 616

Xu, C. & Sulentic, J. W. 1991, ApJ, 374, 407

Xu, C. K., Domingue, D., Cheng, Y., et al. 2010, ApJ, 713, 330

Yang, X., Mo, H. J., van den Bosch, F. C., Pasquali, A., Li, C., & Barden, M. 2007, ApJ, 671, 153

Zuo, P., Xu, C. K., Yun, M. S., Lisenfeld, U., Li, D., & Cao, C. 2018, ApJS, 237, 2